


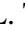


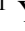


# Timing properties of the X-ray accreting pulsar RX J0440.9+4431 studied with *Insight*-HXMT and NICER

P. P. Li,<sup>1,2</sup> L. Tao <sup>1,\*</sup> Y. L. Tuo <sup>3</sup> M. Y. Ge <sup>1</sup> L. D. Kong <sup>3</sup> L. Zhang,<sup>1</sup> Q. C. Bu <sup>3</sup> L. Ji <sup>4</sup>  
 J. L. Qu,<sup>1</sup> S. Zhang,<sup>1</sup> S. N. Zhang <sup>1</sup> Y. Huang,<sup>1</sup> X. Ma,<sup>1</sup> W. T. Ye,<sup>1,2</sup> Q. C. Zhao,<sup>1,2</sup> R. C. Ma,<sup>1,2</sup>  
 S. J. Zhao,<sup>1,2</sup> X. Hou,<sup>5,6</sup> Z. X. Yang,<sup>7</sup> P. J. Wang,<sup>1,2</sup> S. M. Jia,<sup>1</sup> Q. C. Shui,<sup>1,2</sup> J. Guan,<sup>1</sup>

<sup>1</sup>Key Laboratory of Particle Astrophysics, Institute of High Energy Physics, Chinese Academy of Sciences, 100049 Beijing, People's Republic of China

<sup>2</sup>University of Chinese Academy of Sciences, Chinese Academy of Sciences, 100049 Beijing, People's Republic of China

<sup>3</sup>Institut für Astronomie und Astrophysik, Kepler Center for Astro and Particle Physics, Eberhard Karls Universität, Sand 1, D-72076 Tübingen, Germany

<sup>4</sup>School of Physics and Astronomy, Sun Yat-sen University, Zhuhai, 519082, People's Republic of China

<sup>5</sup>Yunnan Observatories, Chinese Academy of Sciences, Kunming 650216, People's Republic of China

<sup>6</sup>Key Laboratory for the Structure and Evolution of Celestial Objects, Chinese Academy of Sciences, Kunming 650216, People's Republic of China

<sup>7</sup>School of Physics and Optoelectronic Engineering, Shandong University of Technology, Zibo 255000, People's Republic of China

Accepted XXX. Received YYY; in original form ZZZ

## ABSTRACT

RX J0440.9+4431, a Be/X-ray binary, had its brightest outburst in 2022 since its discovery, with a peak X-ray flux of 2.25 Crab (as recorded by *Swift*/BAT, 15–50 keV). We analyze the timing properties of this giant outburst using data from *Insight*-HXMT and *NICER*, focusing on the evolution of the pulse profile and pulse fraction. We observe that when the luminosity reached around  $\sim 3 \times 10^{37}$  erg s<sup>-1</sup>, a transition from double-peaked to single-peaked pulse profiles occurred across the energy range, with the peak of the low-energy profile aligning gradually with the peak of the high-energy profile. This change indicates a transition from subcritical to supercritical accretion. Additionally, we found a concave in the pulse fraction as a function of energy around 20–30 keV throughout the entire outburst period. Compared to the low luminosity, the concave becomes weaker in high luminosities, and overall, the pulse fraction is higher. We propose that this concave could be caused by the scattering of high-energy photons by the atmosphere of a neutron star, leading to a dilution of the pulse fraction. As the accretion reaches the supercritical state, the accretion column height increases, resulting in a larger direct component of strongly beamed X-ray flux, and an elevated pulse fraction.

**Key words:** accretion, accretion disk – X-rays: binaries – stars: neutron-pulsars: individual (RX J0440.9+4431)

## 1 INTRODUCTION

Be/X-ray binaries (BeXRBs) are a subclass of high-mass X-ray binaries (HMXBs). Generally, they consist of a Be star as the companion and a magnetized ( $\geq 10^{12}$  G) neutron star (see reviews by Reig (2011); Mushtukov & Tsygankov (2022)). Be stars are non-supergiant fast-rotating B-type and luminosity class III–V stars. As these stars rotate, they expel matter, giving rise to a disk formation encircling their equator, characterized by emission lines and an excess of infrared radiation (Porter & Rivinius 2003). Generally, BeXRBs are eccentric systems ( $e \geq 0.3$ ) with relatively wide orbits ( $\geq 10$  d). During periastron, the neutron star approaches the circumstellar disk or, regardless of orbital phase, crosses the circumstellar disk, causing significant disruption. Subsequently, a large amount of material is accumulated onto the neutron star. At the magnetospheric radius (Belenkaya et al. 2015), the material is captured by the magnetic field, and the kinetic energy of the falling matter along the magnetic field lines is transformed into radiation, providing energy for X-ray

emission. Misalignment of rotational and magnetic axis results in the phenomenon of X-ray pulsations.

The geometry of the emission region in X-ray pulsars is defined by the magnetic field structure and mass accretion rate. At low luminosities ( $\sim 10^{34-35}$  erg s<sup>-1</sup>), the material passes through a conventional gas-mediated shock, forming a hot spot on the surface of the neutron star, and the emitted radiation escapes from the top of column, forming a "pencil beam" (Nelson et al. 1993). At high luminosities ( $\sim 10^{37-38}$  erg s<sup>-1</sup>), the material encounters a radiation-dominated shock near the top of the accretion column, ultimately settling onto the surface of the neutron star, and the emitted radiation escapes from the walls of the column, forming a "fan beam" (Basko & Sunyaev 1976). In the intermediate range, the emission pattern may be a mixture of these two types (Blum & Kraus 2000; Becker et al. 2012). Naturally, changes in the emission pattern during outbursts lead to variations in the observed pulse profiles. The pulse profiles depend on both the energy band and the accretion luminosity, reflecting the dependence of the beam pattern on the energy and mass accretion rate (see e.g. Tsygankov et al. (2010); Wang et al. (2020, 2022); Rai & Paul (2021a); Hou et al. (2022)). Therefore, investigat-

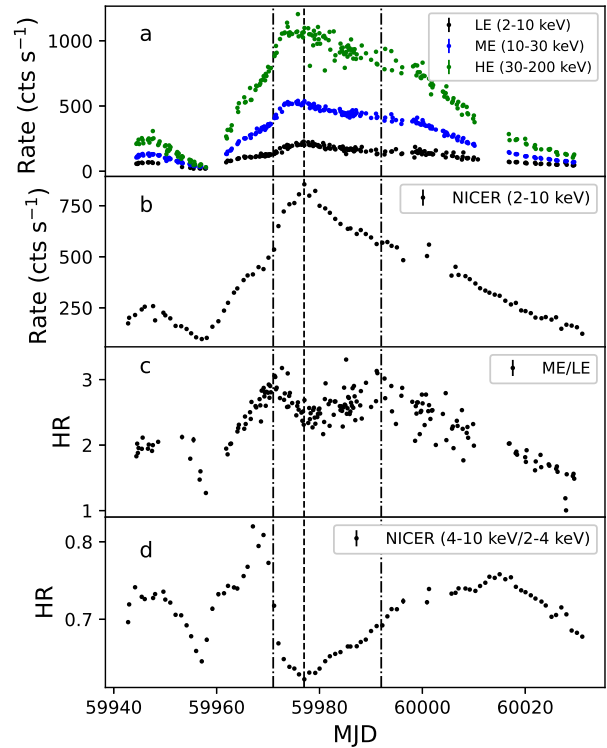
\* E-mail: taolian@ihep.ac.cn

ing pulse profiles provides valuable insights into the understanding of X-ray pulsar accretion mechanisms.

RX J0440.9+4431 was initially discovered as a Be/X-ray binary in the *ROSAT* Galactic plane survey data, and its optical companion was identified as LS V +44 17/BSD 24-491 (Motch et al. 1997). The distance of the source was most recently estimated to be 2.4 kpc (Bailer-Jones et al. 2021). The *RXTE/PCA* was the first to detect X-ray pulsations from RX J0440.9+4431, with a pulse period of  $202.5 \pm 0.5$  s (Reig & Roche 1999). However, subsequent analysis by La Palombara et al. (2012) using *XMM-Newton* data recorded during the RX J0440.9+4431 quiescent states on March 18, 2011, revealed a pulse period of  $204.96 \pm 0.02$  s, indicating an average pulsar spin-down.

RX J0440.9+4431 has experienced three consecutive flux increases until 2022, none of which have a luminosity greater than  $10^{37}$  erg s<sup>-1</sup>. In late March of 2010, the first recorded outburst from RX J0440.9+4431 was detected using the Monitor of All-sky X-ray Image (*MAXI*) instrument (Mori et al. 2010). Then, Usui et al. (2012) analyzed three observations using *RXTE/PCA* and discovered an absorption dip structure at a pulse phase of  $\sim 0.25$  after the main peak in the lower energy bands during an observation that was near the most luminous period of the first outburst. The absorption column density at the dip phase was much higher than those in the other phases. Based on this, Usui et al. (2012) believes that the dip in the pulse profile is caused by the eclipse of radiation from the neutron star by the accretion column. The second outburst from RX J0440.9+4431 was detected by *INTEGRAL* on September 1, 2010, with a luminosity less than half of the previous outburst. According to the analysis conducted by Tsygankov et al. (2012) using data from *Swift/XRT* and *RXTE/PCA*, the pulse profiles exhibit a simple sine-like shape. Additionally, the pulse fraction decreases with decreasing energy in the range of 4–20 keV. Subsequently, in January 2011, the *Swift* observatory detected the third outburst. The recurrence intervals of the three outbursts are approximately 150 days, leading Tsygankov et al. (2012) and Ferrigno et al. (2013) to suggest that the interval may be an orbital period of the binary star, assuming that these outbursts are Type I outbursts that occurred at the periastron passage of the neutron star. However, to accurately determine the orbital parameters of the binary system, much longer observations with high sensitivity and timing accuracy are required.

Eleven years after the third outburst, *MAXI/GSC* detected a brightening of an X-ray source located at RX J0440.9+4431 (Nakajima et al. 2022). Interestingly, towards the end of this outbreak, its count rate increased once again (Pal et al. 2023), reaching a peak X-ray flux of 2.25 Crab (Coley et al. 2023), as recorded by *Swift/BAT* (15–50 keV). This unprecedented event allows for the study of the accretion process of RX J0440.9+4431 across a wider range of luminosity with high-quality data. In this paper, we analyze the dense observations of this source by *Insight-HXMT* and *NICER* to characterize its temporal properties, with a focus on the evolution of pulse profile that is energy and luminosity dependent. From the high-energy data that benefited from *Insight-HXMT*, we can further understand the emission beam pattern of accretion columns in different accretion states. Section 2 presents the observation and data reduction procedures, while Section 3 provides a summary of the results obtained. Finally, Section 4 discusses the findings.



**Figure 1.** Panel a: X-ray light curve of RX J0440.9+4431 by LE (black), ME (blue), and HE (green) with each data binned by one sub-exposure ID (ExpID). Panel b: X-ray light curve of RX J0440.9+4431 in the energy band of 2–10 keV by *NICER* with each data binned by one ObsID. Panel c: Hardness ratio (HR) between 10–30 keV (ME) and 2–10 keV (LE) energy bands using *Insight-HXMT*. Panel d: Hardness ratio between 4–10 keV and 2–4 keV energy bands by *NICER*. Two dashed dotted lines (MJD 59971; MJD 59992) indicate the transition of the pulse profile as shown in Fig. 4. The middle dashed line (MJD 59977) marks the peak of the X-ray light curve for RX J0440.9+4431.

## 2 OBSERVATIONS AND DATA REDUCTION

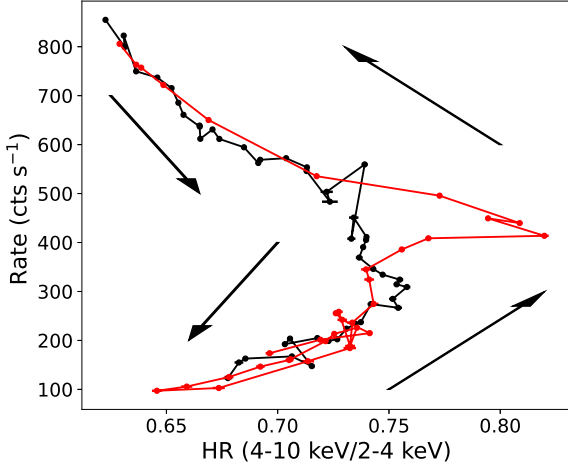
### 2.1 *Insight-HXMT*

The Hard X-ray Modulation Telescope (HXMT), also known as *Insight-HXMT*, is the Chinese first X-ray astronomy satellite with a broad energy in 1–250 keV (Zhang et al. 2020a). It has three main payloads, which are Low Energy X-ray telescope (LE; 1–15 keV), Medium Energy X-ray telescope (ME; 5–30 keV), and High Energy X-ray telescope (HE; 20–250 keV). Starting from December 31, 2022, shortly after the *MAXI* trigger, *Insight-HXMT* commenced its monitoring of RX J0440.9+4431. These observations continued until March 26, 2023, and ObsIDs used in this paper are listed in Table B1.

All observations are analyzed using the *Insight-HXMT* processing software HXMTDAS v2.05<sup>1</sup> to generate clean and calibrated event data, as well as high-level data products such as spectra and light curves<sup>2</sup>. The clean event file of the source is obtained with the following criteria: (1) the Sun Angle  $> 70^\circ$ ; (2) the Moon Angle  $> 6^\circ$ ; (3) the elevation angle  $> 10^\circ$ ; (4) the Cut-off Rigidity value  $> 8$  GV; (5) the pointing offset angle  $< 0.04^\circ$ . In addition, the arrival time of photons in the clean event file is corrected using the *hxbary* tool.

<sup>1</sup> <http://hxmtweb.ihep.ac.cn/software.jhtml>

<sup>2</sup> <http://hxmtweb.ihep.ac.cn/SoftDoc/648.jhtml>



**Figure 2.** The hardness-intensity diagram (HID) of RX J0440.9+4431 in 2022–2023 giant outburst, where the hardness is defined as the count rate ratio of 4–10 to 2–4 keV observed with *NICER*. The black arrows describe the direction of evolution. The red and black colors represent the rising and declining parts of the outburst, respectively.

## 2.2 *NICER*

The Neutron star Interior Composition Explorer (*NICER*) is an instrument onboard the International Space Station (ISS) to study neutron stars in the 0.2–12 keV X-ray band (Gendreau et al. 2016). *NICER* also conducted extensive observations of RX J0440.9+4431 over a period of more than three months, starting on December 29, 2022 and ending on April 15, 2023. This paper uses observations taken before and on March 26, 2023, which are listed in Table B2.

To process these data, we utilize HEASoFT v6.31.1 and the *NICER* Data Analysis Software (NICERDAS 2022-12-16\_v010a) with Calibration Database (CALDB vXTI20221001). The *nicer12* tool is used to implement all standard calibration and screening criteria, producing clean event files. The *barycorr* task is then applied to each clean event file to implement barycentric corrections. Finally, we use a single pipeline task called *nicer13-1c* to extract all light curve products. In order to reduce the impact of background, we examined the light curves of each observation in the 13–15 keV range and removed the times with count rates greater than 1 counts s<sup>-1</sup> (Zhang et al. 2020b).

## 3 ANALYSIS AND RESULTS

### 3.1 Light Curve, Hardness Ratio, and HIDs

Fig. 1 describes the X-ray light curve and hardness ratio (HR) of RX J0440.9+4431 obtained by *Insight*-HXMT and *NICER*. In Panel a, the light curves for three energy bands – LE (2–10 keV), ME (10–30 keV), and HE (30–200 keV) – obtained from *Insight*-HXMT are displayed. Panel b shows the light curve from *NICER* in the energy range of 2–10 keV. The observations of RX J0440.9+4431 by both satellites begin when the count rate of the minor outburst is approaching its peak, with the minor outburst ending on MJD 59958. Subsequently, the count rate rises, and a more extreme outburst ensues. The middle dashed line in Fig. 1 indicates the time of the highest count rate, which occurred on MJD 59977.

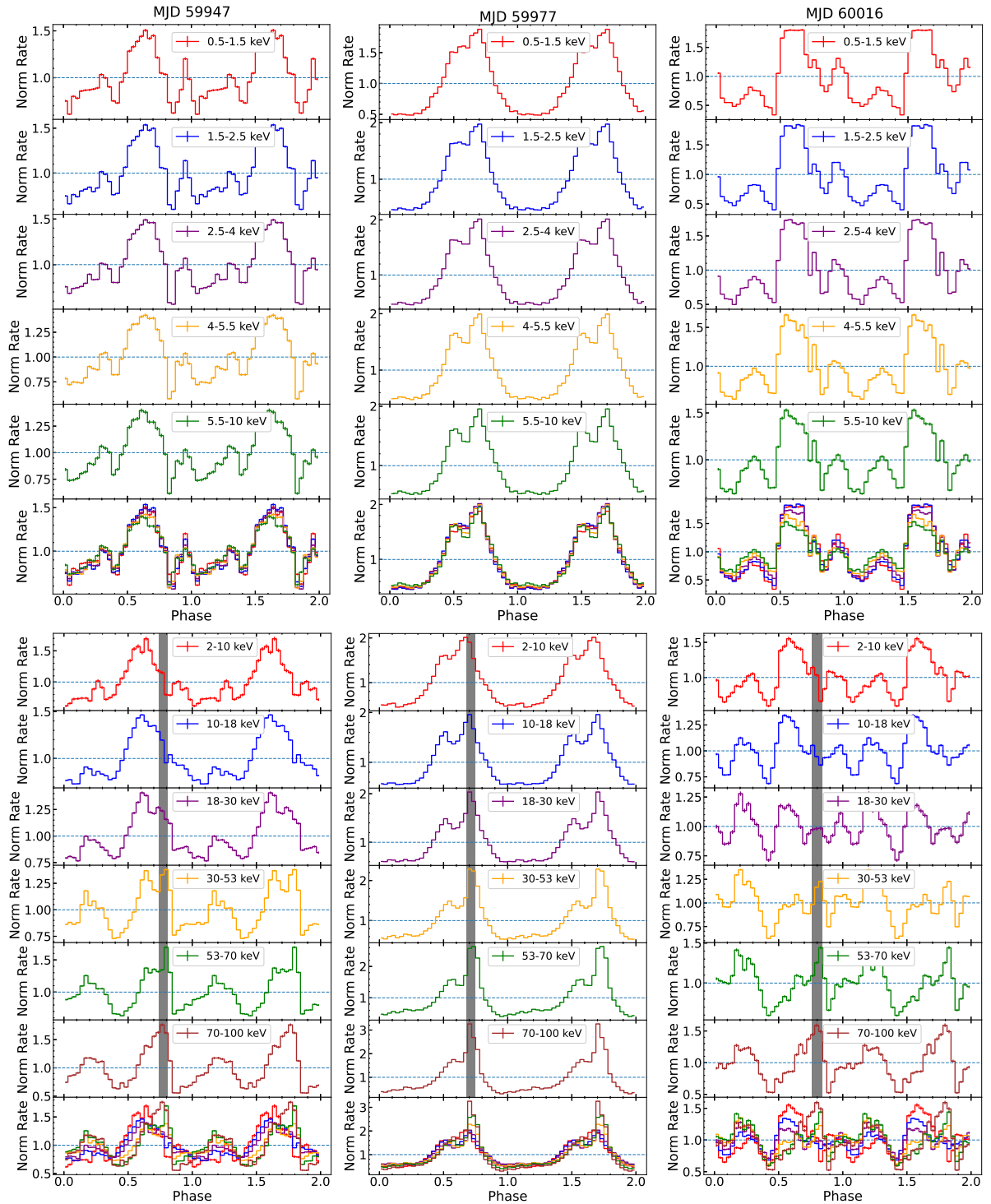
In panel c of Fig. 1, we define the HR as the ratio of 10–30 keV to 2–10 keV energy bands in *Insight*-HXMT. During the minor outburst, the HR increases as the count rate increases and decreases as the count

rate decreases. As the source brightens again, the HR also increases once more. However, at MJD 59971, the hardness ratio begins to decrease. Then, after reaching the minimum around the time of the highest count rate of RX J0440.9+4431, the HR gradually increases again. Finally, HR decreases with a decrease in the count rate at MJD 59992. The panel d is the HR we get using the ratio of 4–10 keV to 2–4 keV of *NICER*, and similar to *Insight*-HXMT, HR decreases when it is MJD 59971, and recovers after the HR reaches its lowest when the source is the brightest. The HR and count rate of *NICER* are plotted in the hardness-intensity diagram (HID) in Fig. 2, with arrows indicating the direction of evolution. The turning in Fig. 2 corresponds to when HR in the panel d in Fig. 1 sharply reduces (~MJD 59971), which aligns with the results presented in Figure 8 by Salganik et al. (2023). This transition may be related to a change in the accretion state of the pulsar, similar to what was found in the Swift J0243.6+6124 (Kong et al. 2020) and RX J0209.6–7427 (Hou et al. 2022).

### 3.2 Evolution of the pulse profile

We analyze observations from both *Insight*-HXMT and *NICER* to study the evolution of the pulse profile of RX J0440.9+4431. Since there are no known orbital elements for the binary system, we do not apply any correction for orbital motion other than barycentric correction. Chi-squared statistics are used to evaluate the best frequency for the pulse of both *Insight*-HXMT and *NICER* observations (Leahy 1987). Subsequently, we fold the net light curves for *Insight*-HXMT observations and the events for *NICER* observations to obtain the pulse profiles. Each pulse profile is divided into 32 bins and normalized by the average source intensity. The cross-correlation method is employed to align the pulse profiles with the reference pulse profile obtained from *NICER*'s ObsID 5203610107 (with an energy range of 0.5–10 keV and pepoch set to MJD 59942).

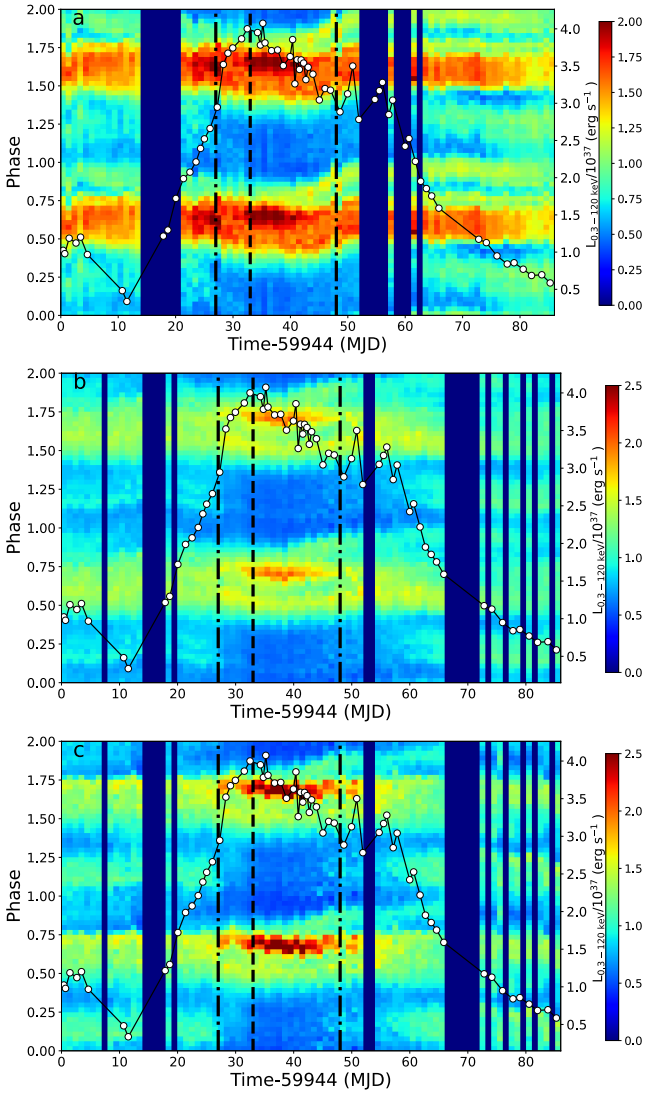
It is widely acknowledged that the pulse profiles of X-ray pulsars are strongly dependent on both energy and luminosity. The resulting evolution of the observed pulse profiles with energy is presented in Fig. 3. The left column shows the observations at MJD 59947. From the low-energy pulse profile given by *NICER*, we can see the dip structure reported in studies of the earlier outbursts at phase 0.81–0.87 (Usui et al. 2012; Tsygankov et al. 2012). Salganik et al. (2023) and Mandal et al. (2023) have also reported this result from their analysis of the *NICER* data for this outburst. In the higher energy pulse profile given by *Insight*-HXMT, this dip does not exist and the minor peak (phases 0.10–0.35) becomes more pronounced with increasing energy. The pulse profiles as a function of energy at the luminosity corresponding to MJD 59947 during the RX J0440.9+4431 decay (MJD 60016) are shown in the right column. Despite the complexity observed in the overall pulse profile compared to the left column, two peaks remain discernible. And the minor peak also demonstrates an increase in intensity with increasing energy. The middle column of Fig. 3 shows the evolution of the pulse profiles when RX J0440.9+4431 is at its brightest. It is evident that the minor peak disappears, and the main peak (phases 0.45–0.75) splits into two wings with a phase separation of about 0.2. As the energy increases, the right wing becomes more prominent, which is consistent with the results presented by Salganik et al. (2023) using *INTEGRAL* and *NuSTAR* data. Furthermore, it is worth noting that in the middle column of Fig. 3, the high-energy (70–100 keV) pulse profile peak and the low-energy (2–10 keV) pulse profile peak are almost in phase. However, there is a phase difference between the high-energy peak and low-energy peak of the low-luminosity pulse profile (the left and right columns).



**Figure 3.** Variation of RX J0440.9+4431 pulse profiles with energy based on observations from *NICER* (top row) and *Insight-HXMT* (ME and HE; bottom row). Each pulse profile is normalized by its mean flux. The three columns from left to right represent pulse profiles from data taken on MJD 59947, MJD 59977, and MJD 60016, respectively. The pulse profiles for different energy ranges are re-plotted in the last row of each panel. The gray shading represents the phase of the peak where the high-energy (70–100 keV) pulse profile is located.

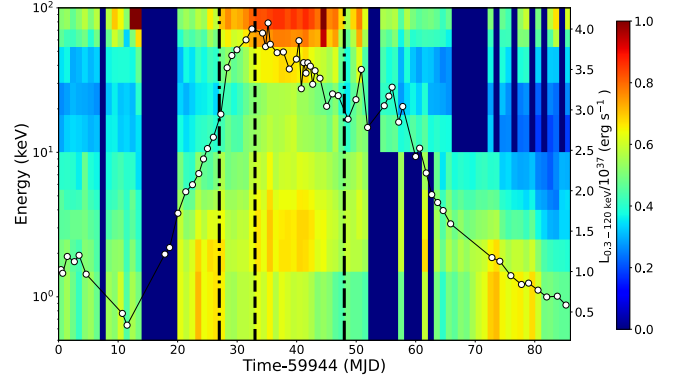
In Fig. 4, we present the phase-time matrix using the normalized pulse profiles for *NICER*, *Insight-HXMT/ME* and *Insight-HXMT/HE*. However, the LE data from *Insight-HXMT* were not included in the presentation due to their inadequate signal-to-noise ratio. The white dots in Fig. 4 correspond to the luminosity in the

energy range of 0.3–120 keV on the right axis, which is calculated using  $cflux$  and assuming a distance of 2.4 kpc after fitting the model:  $Const \times TBabs \times (Gaussian + compTT + compTT)$  (detailed results of *Insight-HXMT* spectra analysis will be reported in the following paper, in preparation). The evolution of the pulse profile from the



**Figure 4.** Panel a: Two-dimensional normalized pulse profiles of RX J0440.9+4431 in the 0.5–10 keV energy band based on *NICER* data. The color bar represents the intensity of the pulse, while the dark blue color indicates that it was not observed during this period. The white dots represent the X-ray luminosity in the energy range of 0.3–120 keV, corresponding to the right y-axis. Two dashed dotted lines (MJD 59971; MJD 59992) indicate the transition of the pulse profile. The second dashed line (MJD 59977) marks the peak of the X-ray light curve for RX J0440.9+4431 in Fig. 1. Panel b: Two-dimensional normalized pulse profiles in the 10–30 keV energy band based on the ME data. Panel c: Two-dimensional normalized pulse profiles in the 30–100 keV energy band based using HE data.

low-energy profile observed by *NICER* to the high-energy profile obtained by *Insight*-HXMT/HE is nearly consistent, as seen in Fig. 4. When the luminosity is below  $\sim 3 \times 10^{37}$  erg s $^{-1}$ , the pulse profile exhibits double peaks, while above  $\sim 3 \times 10^{37}$  erg s $^{-1}$ , it is single-peaked. Two dashed dotted lines (MJD 59971; MJD 59992) in Fig. 4 correspond to the time points of the pulse profile transition. In panel c of Fig. 1, the HR also exhibits a transition at these same two dashed dotted lines. It is worth noting that when the luminosity is less than  $3 \times 10^{37}$  erg s $^{-1}$ , the dip structure appears at a phase of about 0.8 in the soft energy pulse profile (Panel a of Fig. 4). Before MJD 59977, there was no dip in the hard energy range, consistent with previous reports. However, after MJD 59992, the main peak in the high-energy



**Figure 5.** Two-dimensional pulsed fraction of RX J0440.9+4431 based on the *NICER* and *Insight*-HXMT. Data points below 10 keV are from *NICER*, while the other data points are from ME and HE. The energy range divisions are the same as shown in Fig. 3. The black dashed lines and white circles are the same as in Fig. 4. The points in extreme reddish-brown color due to using the net light curve to fold the pulse profile for *Insight*-HXMT, resulting in negative counts and pulsar fraction larger than 1.

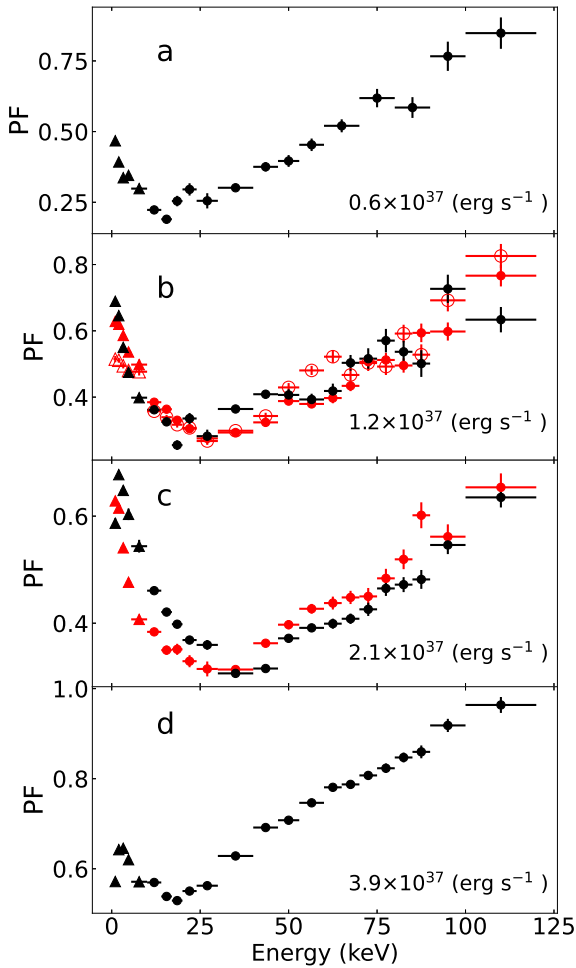
range also exhibited splitting at a phase of about 0.8 (Panel c of Fig. 4), which is difficult to explain using the explanations for the dip structure in the soft energy range.

### 3.3 Evolution of the pulsed fraction

To quantify the pulse intensity, we calculated the pulsed fraction (PF) of RX J0440.9+4431:

$$PF = (F_{\max} - F_{\min}) / (F_{\max} + F_{\min}), \quad (1)$$

where  $F_{\max}$  and  $F_{\min}$  are the maximum and minimum fluxes in the pulse profile, respectively. The energy-time matrix using the pulsed fraction for *NICER* and *Insight*-HXMT is shown in Fig. 5. The white dots and three black lines are the same as in Fig. 1 and Fig. 4. During the outburst, the PF is at its lowest around  $\sim 20$ – $30$  keV, which aligns with the findings reported by Salganik et al. (2023) based on the analysis of *NuSTAR* data. In Figure 5 of Salganik et al. (2023), the PF for low luminosities does not appear as smooth around  $\sim 60$  keV. Benefiting from the large effective area of *Insight*-HXMT and its dense observations of RX J0440.9+4431, we have subdivided the energy ranges further, and Fig. 6 depicts the variations in PF with energy for four different luminosity levels. In panels b and c, there is a less pronounced increase in the PF around  $\sim 60$  keV. This behavior is not observed in panels a and d. Furthermore, the PF in panel d is larger than the other panels. This suggests a correlation between the PF and the luminosity (Mushtukov et al. 2018; Wang et al. 2020, 2022). Therefore, we plot the variation of the PF with luminosity for RX J0440.9+4431 using *NICER* and *Insight*-HXMT data in Fig. 7. From panels a (2–10 keV) and b (10–30 keV) of Fig. 7, it can be seen that the PF is positively correlated with the luminosity. However, in the falling phase of the outburst, the relationship between the PF and luminosity is steeper compared to the rising phase. Moreover, for panel c (30–100 keV) from the high-energy range, unlike panels a and b, the PF exhibits a slight negative correlation at low luminosity and a positive correlation at high luminosity, and the rising and falling phases of the outburst are similar.



**Figure 6.** Pulsed fraction of RX J0440.9+4431 as a function of energy at different luminosities using *NICER* (triangle mark) and *Insight-HXMT* (circle mark) data. The red and black colors represent the rising and declining parts of the outburst, respectively. The hollow circles are derived from data prior to MID 59958.

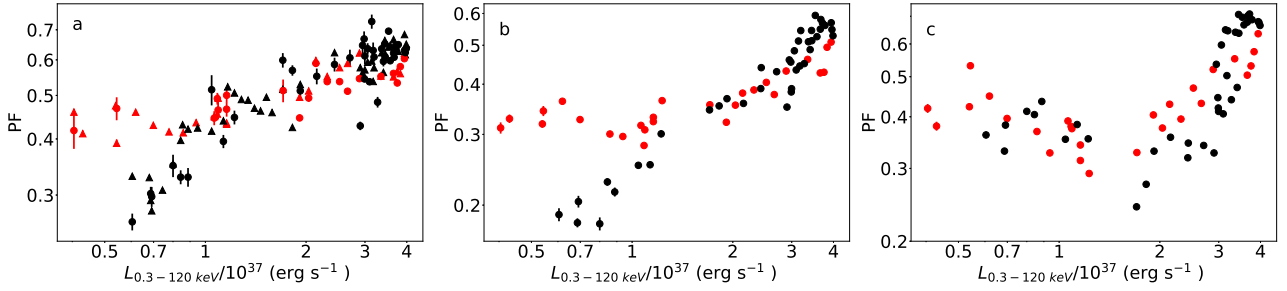
#### 4 DISCUSSION AND CONCLUSION

We conduct an analysis of the *NICER* and *Insight-HXMT* data for the RX J0440.9+4431 giant outburst during 2022–2023, with a focus on the timing properties. The research further supplements the understanding of the timing properties in higher energy ranges. Prior to our study, [Salganik et al. \(2023\)](#) had analyzed the *NICER* data and provided a comprehensive evolution of the low-energy pulse profile. They found that the pulse profile undergoes a transition from a double-peak pattern to a single-peak pattern at a luminosity of  $\sim 2.8 \times 10^{37} \text{ erg s}^{-1}$ , which was considered to be the critical luminosity. Additionally, [Mandal et al. \(2023\)](#) also found that the spectral parameters obtained from *NICER* observations undergo changes at this luminosity. Above this luminosity, the correlation between the photon index and flux becomes positive, and the cut-off energy also increases with the increasing flux. We present a more complete evolution of the mid-energy (10–30 keV) and high-energy (30–100 keV) pulse profiles, revealing that they also transition from a double-peak pattern to a single-peak pattern around a luminosity of  $\sim 3 \times 10^{37} \text{ erg s}^{-1}$ , consistent with the low-energy evolution. The results suggest a significant alteration in the radiation beam, indicating the existence of different accretion regimes ([Reig & Nespoli](#)

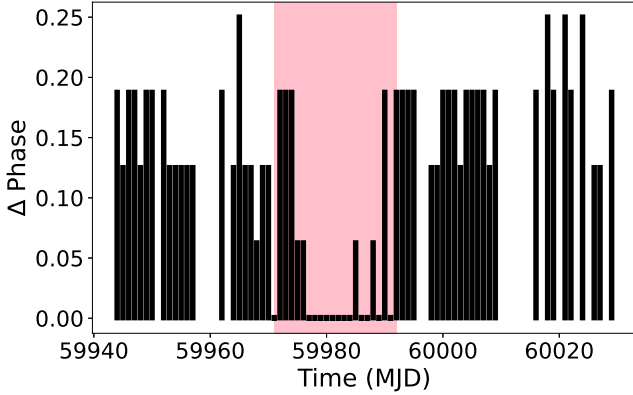
2013). These regimes are defined by a critical luminosity ( $L_{\text{crit}}$ ), which represents the luminosity at which the radiation pressure primarily begins to decelerates the accreting material above the neutron star. The changes in the radiation beam are typically accompanied by a change in the pulse profile shape and the spectral shape, as observed in other sources such as 1A 0535+262 ([Wang et al. 2022](#)), EXO 2030+375 ([Fu et al. 2023](#)), 4U 1901+03 ([Tuo et al. 2020](#)), RX J0209.6-7427 ([Hou et al. 2022](#)), and Swift J0243.6+6124 ([Liu et al. 2022](#)).

Additionally, benefiting from the high HXMT statistics and broad energy range, during high luminosity, we can observe that the peaks of the high-energy and low-energy pulse profiles coincide, indicating that they both originate from the same direction, as seen in the middle column of Fig. 3. Conversely, when the luminosity is low, the phase of the peak in the low-energy pulse profile differs from that of the peak in the high-energy pulse profile. This suggests that high-energy photons and low-energy photons are not emitted from the same direction. This feature was previously proposed in the pulse profile evolution of EXO 2030+375, where [Fu et al. \(2023\)](#) utilized the phase difference between the high-energy and low-energy pulse peaks to determine the critical luminosity during its 2021 giant outburst. To track the temporal evolution of the phase difference between the high-energy and low-energy pulse profile peaks in RX J0440.9+4431, we divide one pulse period into 16 bins to individually fold the profiles. This division helps mitigate occasional data point jumps caused by localized profile features. We compute  $\Delta \text{Phase}$  corresponding to the maximum values of the high-energy (70–100 keV) and low-energy (10–18 keV) pulse profiles. The final results are presented in Fig. 8. From Fig. 8, we can see that within the red shaded region where the luminosity is greater than  $3 \times 10^{37} \text{ erg s}^{-1}$ ,  $\Delta \text{Phase}$  is very small, and the peak of the high-energy profile aligns closely with the peak of the low-energy profile in phase. As discussed by [Hou et al. \(2022\)](#), during high luminosity, both low-energy and high-energy photons mainly escape from the sides of the accretion column. There is a jump from 0 to 0.1875 at the start and end positions of the red shadow. Further examination of the pulse profile in the 10–18 keV range reveal that the main peak splits into two wings, and these two wings have similar magnitudes. Therefore, during the transition from the left-dominant wing to the right-dominant wing in the pulse profile of the main peak, even slight instability can cause a phase jump. At higher luminosities, the low-energy pulse profile is completely dominated by the right-side swing, resulting in almost overlapping pulse peaks for high-energy and low-energy, as shown in Fig. 3. The critical luminosity obtained using this method is consistent with the results obtained from the transition of the pulse profile from single to double peaks and the evolution of the energy spectra. This further validates the feasibility of using this method to determine the critical luminosity.

[Lutovinov & Tsygankov \(2009\)](#) investigated the ten brightest X-ray pulsars using *INTEGRAL* data in the hard ( $> 20 \text{ keV}$ ) energy band and found that the pulse fraction increases with energy for all pulsars. Subsequently, similar findings of PF increasing with energy were reported in pulsars such as 2S 1845–024 ([Nabizadeh et al. 2022](#)) GRO J2058+42 ([Gorban et al. 2022](#)), 1A 0535+262 ([Wang et al. 2022](#)), Swift J1808.4–1754 ([Salganik et al. 2022a](#)), Swift J1626.6–5156 ([Molkov et al. 2021](#)), XTE J1858+034 ([Tsygankov et al. 2021](#)), 4U 1901+03 ([Rai & Paul 2021b](#)), eRASSU J050810.4–660653 ([Salganik et al. 2022b](#)), Swift J1816.7–1613 ([Nabizadeh et al. 2019](#)), etc. High-energy photons have a significantly larger optical depth along the magnetic field direction, allowing them to escape only from the sides of the accretion column. In contrast, low-energy photons have less restricted escape directions and can exit both from



**Figure 7.** Panel a: Pulsed fraction of RX J0440.9+4431 as a function of luminosity in the 2–10 keV energy range using *NICER* (triangle mark) and *Insight-HXMT* (circle mark) data. The red and black data points represent the data before and after the source reaches its peak luminosity, respectively. Panel b: Pulsed fraction in the 10–30 keV energy range from ME. Panel c: Pulsed fraction in the 30–100 keV energy range from HE.



**Figure 8.** The temporal evolution of the phase difference between the high-energy (70–100 keV) and low-energy (10–18 keV) pulse profile peaks. The start and end positions of the red shaded region correspond to the dashed lines in Fig. 4.

the sides and the top of the column (Hou et al. 2022). This leads to a more concentrated emission for higher-energy radiation compared to lower-energy radiation, which provides a possible explanation for the increase in pulse fraction with energy for high-energy photons. In addition, Lutovinov & Tsygankov (2009) also found that in many cases, this increase is not monotonic, exhibiting local features near the cyclotron line harmonics. As shown in Fig. 5 and Fig. 6, there is a prominent concave in the PF at  $\sim 20$ –30 keV for RX J0440.9+4431, but no cyclotron absorption lines were detected in its spectra (Salganik et al. 2023). During the outburst in September 2010, Tsygankov et al. (2012) reported the discovery of a possible cyclotron absorption line at 32 keV in RX J0440.9+4431. Notably, Fig. 6 reveals the PF does not appear to increase smoothly with energy at the first harmonic of the cyclotron absorption line. However, when we use the RMS pulse fraction calculated using equation A.3 from Ferrigno et al. (2023) to quantify the pulse profile, this feature becomes less prominent (Fig. A1). Consequently, it is difficult to consider the possibility that these features are attributed to the effects of resonant absorption. It may be worth considering the use of the more precise PF spectrum proposed by Ferrigno et al. (2023) in the subsequent work. At the low luminosity, 1A 0535+262 exhibits a prominent concave in the PF around 20–30 keV, which Chhotaray et al. (2023) attributed this concave to the diffused X-ray emission from the relatively hot plasma above the pole of the neutron star. Postnov et al. (2015) and Kylafis et al. (2021) studied the reflection of continuum X-ray photons at the atmosphere of a magnetic neutron star. At low and high energies, the reflected spectra

are significantly reduced due to absorption and downward scattering, resulting in a prominent bump around 20–30 keV. The process of reflection redistributes the emitted photons, leading us to hypothesize that the decreased PF at  $\sim 20$ –30 keV may arise from the dilution of reflected photons. The proportion of reflected photons affects the depth of the concave, and this proportion is related to the height of the accretion column (Poutanen et al. 2013). A higher accretion column results in a lower probability of photon scattering. Above the critical luminosity, the concave is weaker, which may suggest a lower proportion of reflected photons and a higher accretion column compared to the low luminosity.

As shown above, the pulse profiles and pulse fractions of X-ray pulsars exhibit a dependency on their luminosity. In Fig. 7, a transition in the pulse fraction variation with luminosity occurs at a luminosity of  $\sim 2 \times 10^{37}$  erg s $^{-1}$ . This luminosity is very close to the critical luminosity defined in our study. Above this luminosity, the pulse fraction increases with increasing luminosity for high-energy, medium-energy, and low-energy photons. Below this luminosity, the pulse fraction for high-energy photons shows consistent variations with luminosity in the rising and falling phases. However, for low-energy photons, the pulse fraction in the falling phase is lower than that in the rising phase. This discrepancy can be attributed to the fact that while high-energy photons predominantly originate from the polar caps via direct emission, low-energy photons comprise contributions from direct emission, thermal components, and downward scattering of high-energy photons. This implies that the generation process of low-energy photons may differ between the rising and falling phases. Inconsistencies in the physical parameters at the same luminosity during the rising and falling phases have been observed in other sources, such as 1A 0535+262 (Kong et al. 2021) and V 0332+53 (Doroshenko et al. 2017), in terms of cyclotron absorption line energies. These discrepancies have been explained as possibly being related to the geometric shape of the radiation region during the rising and falling phases, potentially caused by changes in the accretion disk structure and its interaction with the magnetosphere of the neutron star. However, the exact cause of these differences is not yet well understood.

Currently, our understanding of the accretion physics in X-ray pulsars is still limited. The pulse profile is influenced by various factors such as the viewing angle to the magnetic pole, the distribution of radiation beams, and relativistic effects. The temporal properties of X-ray accreting pulsars require further investigation through detailed simulations and higher-quality observational data in the future.

**ACKNOWLEDGEMENTS**

This research utilized data and software from the High Energy Astrophysics Science Archive Research Center (HEASARC), provided by NASA's Goddard Space Flight Center, as well as the *Insight-HXMT* mission, supported by the China National Space Administration (CNSA) and the Chinese Academy of Sciences (CAS). This work is supported by the National Key R&D Program of China (2021YFA0718500). We acknowledge funding support from the National Natural Science Foundation of China (NSFC) under grant No. 12122306, No. U2038102, No. U2031205, No. U2038104, No. U1838201, No. U1838108, No. 12173103, No. 12041303, the CAS Pioneer Hundred Talent Program Y8291130K2 and the Scientific and technological innovation project of IHEP Y7515570U1.

**DATA AVAILABILITY**

The data of *insight-HXMT* can be obtained from this website <http://hxmtweb.ihep.ac.cn/>. The data of *NICER* used for this paper are publicly available in the High Energy Astrophysics Science Archive Research Centre (HEASARC) at <https://heasarc.gsfc.nasa.gov/cgi-bin/W3Browse/w3browse.pl>.

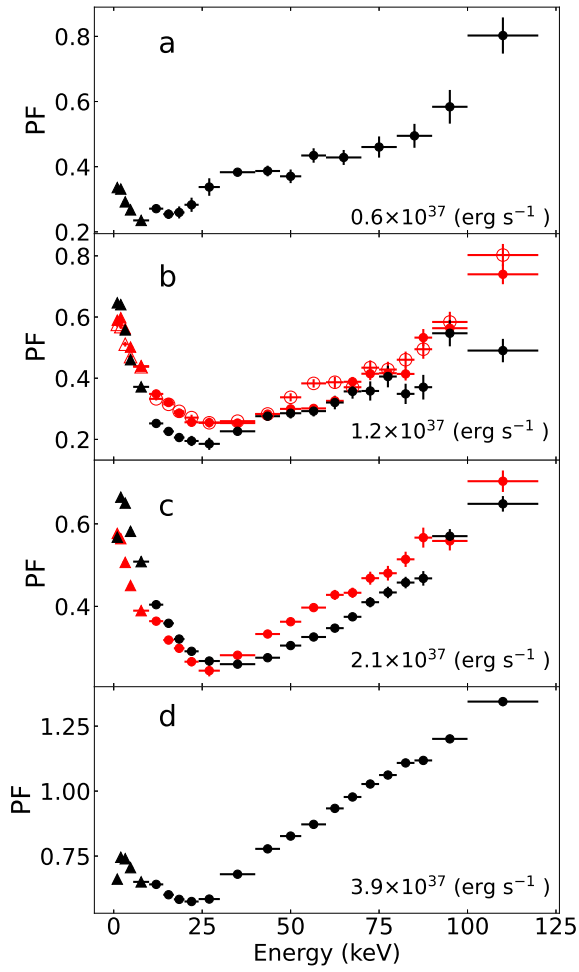
**REFERENCES**

- Bailer-Jones C. A. L., Rybizki J., Foesneau M., Demleitner M., Andrae R., 2021, *VizieR Online Data Catalog*, p. [I/352](#)
- Basko M. M., Sunyaev R. A., 1976, *MNRAS*, **175**, 395
- Becker P. A., et al., 2012, *A&A*, **544**, [A123](#)
- Belenkaya E. S., Khodachenko M. L., Alexeev I. I., 2015, in Lammer H., Khodachenko M., eds, *Astrophysics and Space Science Library* Vol. 411, *Characterizing Stellar and Exoplanetary Environments*. p. 239, [doi:10.1007/978-3-319-09749-7\\_12](https://doi.org/10.1007/978-3-319-09749-7_12)
- Blum S., Kraus U., 2000, *ApJ*, **529**, 968
- Chhotaray B., Jaisawal G. K., Kumari N., Naik S., Kumar V., Jana A., 2023, *MNRAS*, **518**, 5089
- Coley J. B., et al., 2023, *The Astronomer's Telegram*, **15907**, 1
- Doroshenko V., Tsygankov S. S., Mushtukov A. A., Lutovinov A. A., Santangelo A., Suleimanov V. F., Poutanen J., 2017, *MNRAS*, **466**, 2143
- Ferrigno C., Farinelli R., Bozzo E., Pottschmidt K., Klochov D., Kretschmar P., 2013, *A&A*, **553**, [A103](#)
- Ferrigno C., D'Ài A., Ambrosi E., 2023, *arXiv e-prints*, p. [arXiv:2308.03395](#)
- Fu Y.-C., et al., 2023, *MNRAS*, **521**, 893
- Gendreau K. C., et al., 2016, in den Herder J.-W. A., Takahashi T., Bautz M., eds, *Society of Photo-Optical Instrumentation Engineers (SPIE) Conference Series* Vol. 9905, *Space Telescopes and Instrumentation 2016: Ultraviolet to Gamma Ray*. p. 99051H, [doi:10.1117/12.2231304](https://doi.org/10.1117/12.2231304)
- Gorban A. S., Molkov S. V., Tsygankov S. S., Mushtukov A. A., Lutovinov A. A., 2022, *Astronomy Letters*, **48**, 256
- Hou X., et al., 2022, *ApJ*, **938**, 149
- Kong L. D., et al., 2020, *ApJ*, **902**, 18
- Kong L. D., et al., 2021, *ApJ*, **917**, [L38](#)
- Kylafis N. D., Trümper J. E., Loudas N. A., 2021, *A&A*, **655**, [A39](#)
- La Palombara N., Sidoli L., Esposito P., Tiengo A., Mereghetti S., 2012, *A&A*, **539**, [A82](#)
- Leahy D. A., 1987, *A&A*, **180**, 275
- Liu J., et al., 2022, *MNRAS*, **512**, 5686
- Lutovinov A. A., Tsygankov S. S., 2009, *Astronomy Letters*, **35**, 433
- Mandal M., et al., 2023, *arXiv e-prints*, p. [arXiv:2306.08083](#)
- Molkov S., Doroshenko V., Lutovinov A., Tsygankov S., Santangelo A., Mereminskiy I., Semena A., 2021, *ApJ*, **915**, [L27](#)
- Morii M., et al., 2010, *The Astronomer's Telegram*, **2527**, 1
- Motch C., Haberl F., Dennerl K., Pakull M., Janot-Pacheco E., 1997, *A&A*, **323**, 853

- Mushtukov A., Tsygankov S., 2022, *arXiv e-prints*, p. [arXiv:2204.14185](#)
- Mushtukov A. A., Verhagen P. A., Tsygankov S. S., van der Klis M., Lutovinov A. A., Larchenkova T. I., 2018, *MNRAS*, **474**, 5425
- Nabizadeh A., Tsygankov S. S., Karasev D. I., Mönkkönen J., Lutovinov A. A., Nagirner D. I., Poutanen J., 2019, *A&A*, **622**, [A198](#)
- Nabizadeh A., Tsygankov S. S., Molkov S. V., Karasev D. I., Ji L., Lutovinov A. A., Poutanen J., 2022, *A&A*, **657**, [A58](#)
- Nakajima M., et al., 2022, *The Astronomer's Telegram*, **15835**, 1
- Nelson R. W., Salpeter E. E., Wasserman L., 1993, *ApJ*, **418**, 874
- Pal S., et al., 2023, *The Astronomer's Telegram*, **15868**, 1
- Porter J. M., Rivinius T., 2003, *PASP*, **115**, 1153
- Postnov K. A., Gornostaev M. I., Klochov D., Laplace E., Lukin V. V., Shakura N. I., 2015, *MNRAS*, **452**, 1601
- Poutanen J., Mushtukov A. A., Suleimanov V. F., Tsygankov S. S., Nagirner D. I., Doroshenko V., Lutovinov A. A., 2013, *ApJ*, **777**, 115
- Rai B., Paul B. C., 2021a, *Ap&SS*, **366**, 84
- Rai B., Paul B. C., 2021b, *Ap&SS*, **366**, 84
- Reig P., 2011, *Ap&SS*, **332**, 1
- Reig P., Nespoli E., 2013, *A&A*, **551**, [A1](#)
- Reig P., Roche P., 1999, *MNRAS*, **306**, 100
- Salganik A., Tsygankov S. S., Lutovinov A. A., Djupvik A. A., Karasev D. I., Molkov S. V., 2022a, *MNRAS*, **514**, 2707
- Salganik A., Tsygankov S. S., Lutovinov A. A., Mushtukov A. A., Mereminskiy I. A., Molkov S. V., Semena A. N., 2022b, *MNRAS*, **514**, 4018
- Salganik A., Tsygankov S. S., Doroshenko V., Molkov S. V., Lutovinov A. A., Mushtukov A. A., Poutanen J., 2023, *arXiv e-prints*, p. [arXiv:2304.14881](#)
- Tsygankov S. S., Lutovinov A. A., Serber A. V., 2010, *MNRAS*, **401**, 1628
- Tsygankov S. S., Krivonos R. A., Lutovinov A. A., 2012, *MNRAS*, **421**, 2407
- Tsygankov S. S., et al., 2021, *ApJ*, **909**, 154
- Tuo Y. L., et al., 2020, *Journal of High Energy Astrophysics*, **27**, 38
- Usui R., et al., 2012, *PASJ*, **64**, 79
- Wang P. J., et al., 2020, *MNRAS*, **497**, 5498
- Wang P. J., et al., 2022, *ApJ*, **935**, 125
- Zhang S.-N., et al., 2020a, *Science China Physics, Mechanics, and Astronomy*, **63**, 249502
- Zhang L., et al., 2020b, *MNRAS*, **499**, 851

**APPENDIX A: FIGURES****APPENDIX B: TABLES**





**Figure A1.** The RMS pulse fraction of RX J0440.9+4431 as a function of energy at different luminosities using *NICER* (triangle mark) and *Insight-HXMT* (circle mark) data. The red and black colors represent the rising and declining parts of the outburst, respectively. The hollow circles are derived from data prior to MID 59958.

Table B1: *Insight*-HXMT observations log used in this paper. The net count rates in the HE band (30–100 keV) and the periods are listed.

ObsIDs	ExpIDs	Start Time (MJD)	HE Exposure Time (s)	HE Count Rate (cts s <sup>-1</sup> )	Period (s)
P0514361001	P051436100101	59944.40	1971	181.1 ± 0.3	208.73 ± 1.80
	P051436100102	59944.56	4298	177.5 ± 0.2	
	P051436100104	59944.82	3290	204.9 ± 0.2	208.01 ± 0.67
	P051436100105	59944.96	2389	175.2 ± 0.3	
P0514361002	P051436100201	59945.46	4467	210.3 ± 0.2	207.98 ± 0.55
	P051436100202	59945.62	2082	200.3 ± 0.3	
	P051436100203	59945.75	578	180.2 ± 0.6	
P0514361003	P051436100301	59946.65	1125	203.7 ± 0.4	207.87 ± 0.48
	P051436100302	59946.81	3444	208.6 ± 0.2	
	P051436100303	59946.94	2351	180.6 ± 0.3	
P0514361004	P051436100401	59947.44	5129	206.6 ± 0.2	208.03 ± 0.45
	P051436100402	59947.60	169	258.4 ± 1.2	
	P051436100403	59947.73	741	213.9 ± 0.5	
P0514361005	P051436100501	59948.63	1636	172.7 ± 0.3	207.84 ± 0.49
	P051436100502	59948.79	3381	181.2 ± 0.2	
	P051436100503	59948.92	2296	189.7 ± 0.3	
P0514361008	P051436100801	59949.95	4681	160.1 ± 0.2	207.79 ± 0.63
	P051436100802	59950.11	1789	164.9 ± 0.3	
	P051436100803	59950.24	1001	110.8 ± 0.3	
	P051436100804	59950.37	3932	129.3 ± 0.2	207.92 ± 0.45
	P051436100805	59950.51	2623	141.7 ± 0.2	
	P051436100806	59950.64	1189	133.1 ± 0.3	
	P051436100807	59950.77	3276	164.8 ± 0.2	207.84 ± 0.47
	P051436100808	59950.91	3420	138.5 ± 0.2	
	P051436100809	59951.04	2976	154.4 ± 0.2	
P0514361009	P051436100901	59952.20	698	124.3 ± 0.4	208.00 ± 0.64
	P051436100902	59952.36	4083	122.7 ± 0.2	
	P051436100903	59952.49	1511	93.7 ± 0.2	208.04 ± 2.13
	P051436100904	59952.63	522	115.5 ± 0.5	
P0514361015	P051436101501	59953.13	1227	86.9 ± 0.3	207.91 ± 1.65
	P051436101502	59953.28	2026	98.3 ± 0.2	
	P051436101503	59953.42	2768	90.5 ± 0.2	
P0514361016	P051436101601	59954.72	2983	79.7 ± 0.2	207.39 ± 2.01
	P051436101602	59954.87	3041	59.2 ± 0.1	
	P051436101603	59955.01	1554	74.3 ± 0.2	
P0514361017	P051436101701	59955.51	576	51.0 ± 0.3	207.91 ± 2.02
	P051436101702	59955.67	2578	65.0 ± 0.2	
	P051436101703	59955.80	1526	50.3 ± 0.2	
P0514361018	P051436101801	59956.70	3657	38.9 ± 0.1	207.59 ± 1.08
	P051436101802	59956.86	1473	44.2 ± 0.2	
	P051436101803	59956.98	929	51.6 ± 0.2	
P0514361019	P051436101901	59957.63	3311	33.1 ± 0.1	...
	P051436101902	59957.78	2841	35.7 ± 0.1	
	P051436101903	59957.91	1398	31.1 ± 0.1	
P0514361022	P051436102201	59961.86	1403	218.1 ± 0.4	...
	P051436102202	59962.00	584	201.8 ± 0.6	
	P051436102203	59962.13	1344	255.0 ± 0.4	
P0514361023	P051436102301	59962.65	3289	262.2 ± 0.3	207.70 ± 0.44
	P051436102302	59962.81	1941	255.4 ± 0.4	
	P051436102303	59962.94	691	284.6 ± 0.6	
P0514361024	P051436102401	59964.04	925	397.7 ± 0.7	207.65 ± 0.58
	P051436102402	59964.19	3989	368.9 ± 0.3	
	P051436102403	59964.33	947	421.9 ± 0.7	
P0514361025	P051436102501	59965.37	871	454.3 ± 0.7	207.59 ± 0.48
	P051436102502	59965.52	2015	426.3 ± 0.5	
	P051436102503	59965.65	2240	429.8 ± 0.4	

to be continued

ObsIDs	ExpIDs	Start time (MJD)	Exposure time (s)	Count Rate (cts s <sup>-1</sup> )	Period (s)
P0514361026	P051436102601	59966.50	2315	519.6 ± 0.5	207.58 ± 0.55
	P051436102602	59966.64	2193	442.7 ± 0.4	
	P051436102603	59966.77	803	441.2 ± 0.7	
P0514361027	P051436102701	59967.56	2248	506.6 ± 0.5	207.59 ± 0.58
	P051436102702	59967.70	1619	535.6 ± 0.6	
	P051436102703	59967.83	399	531.1 ± 1.2	
P0514361028	P051436102801	59968.35	1068	540.1 ± 0.7	207.52 ± 0.42
	P051436102802	59968.49	2227	549.0 ± 0.5	
	P051436102803	59968.62	2134	567.6 ± 0.5	
P0514361029	P051436102901	59969.01	1757	569.1 ± 0.6	207.43 ± 0.21
	P051436102902	59969.14	3288	594.2 ± 0.4	
	P051436102904	59969.42	2185	565.1 ± 0.5	
	P051436102905	59969.55	2482	603.5 ± 0.5	
	P051436102906	59969.68	2061	593.5 ± 0.5	
P0514361030	P051436103001	59970.00	2144	649.2 ± 0.6	207.39 ± 0.26
	P051436103002	59970.14	3197	618.7 ± 0.4	
	P051436103005	59970.54	2518	638.9 ± 0.5	
	P051436103006	59970.68	2009	745.7 ± 0.6	
P0514361031	P051436103101	59971.26	571	719.2 ± 1.1	207.36 ± 0.41
	P051436103102	59971.41	2415	728.4 ± 0.5	
	P051436103103	59971.54	2657	776.3 ± 0.5	
	P051436103104	59971.67	1163	732.3 ± 0.8	
P0514361032	P051436103201	59972.32	7350	812.7 ± 0.3	207.31 ± 0.43
	P051436103202	59972.70	601	843.1 ± 1.2	
P0514361035	P051436103501	59973.11	2296	844.8 ± 0.6	207.12 ± 0.19
	P051436103502	59973.25	7933	846.7 ± 0.3	
	P051436103503	59973.69	918	909.6 ± 1.0	
	P051436103504	59973.82	542	882.9 ± 1.3	
	P051436103505	59973.96	4329	844.7 ± 0.4	
	P051436103506	59974.10	2277	832.5 ± 0.6	
	P051436103507	59974.24	13379	848.9 ± 0.3	
	P051436103508	59974.69	3740	840.5 ± 0.5	
P0514361036	P051436103601	59975.49	6608	849.9 ± 0.4	206.99 ± 0.28
	P051436103602	59975.68	3068	851.9 ± 0.5	
	P051436103603	59975.80	446	965.9 ± 1.5	
	P051436103604	59975.94	5930	824.9 ± 0.4	
P0514361037	P051436103701	59976.48	6960	829.6 ± 0.3	206.85 ± 0.23
	P051436103702	59976.67	3084	849.1 ± 0.5	
	P051436103703	59976.79	538	820.1 ± 1.2	
	P051436103704	59976.93	6110	848.8 ± 0.4	
	P051436103705	59977.08	2106	878.5 ± 0.6	
P0514361038	P051436103801	59977.80	3828	876.5 ± 0.5	206.78 ± 0.41
	P051436103802	59978.00	4776	839.9 ± 0.4	
	P051436103803	59978.14	549	645.6 ± 1.1	
	P051436103804	59978.27	13297	837.6 ± 0.3	
	P051436103805	59978.65	3113	828.4 ± 0.5	
	P051436103806	59978.78	833	781.5 ± 1.0	
	P051436103807	59978.92	6286	860.1 ± 0.4	
	P051436103808	59979.06	1285	813.1 ± 0.8	
	P051436103809	59979.20	10514	838.8 ± 0.3	
	P051436103810	59979.57	3059	781.1 ± 0.5	
	P051436103811	59979.70	1482	886.5 ± 0.8	
	P051436103812	59979.83	4536	811.8 ± 0.4	
	P051436103813	59979.98	3618	846.4 ± 0.5	
	P051436103814	59980.12	950	782.7 ± 0.9	
P0514361040	P051436104001	59980.71	2681	824.9 ± 0.6	206.46 ± 0.29
	P051436104002	59980.90	5392	832.0 ± 0.4	
	P051436104003	59981.04	19	654.3 ± 5.9	
	P051436104004	59981.18	2738	813.6 ± 0.5	

to be continued

ObsIDs	ExpIDs	Start time (MJD)	Exposure time (s)	Count Rate (cts s <sup>-1</sup> )	Period (s)	
P0514361041	P051436104101	59981.77	3100	804.5 ± 0.5	206.40 ± 0.29	
	P051436104102	59981.96	1521	854.8 ± 0.7		
	P051436104103	59982.10	3514	746.7 ± 0.5		
P0514361042	P051436104201	59982.76	2674	861.8 ± 0.6	206.34 ± 0.32	
	P051436104202	59982.95	1082	680.0 ± 0.8		
	P051436104203	59983.09	3452	719.2 ± 0.5		
P0514361043	P051436104301	59983.95	670	734.2 ± 1.0	206.28 ± 0.39	
	P051436104302	59984.08	2011	786.1 ± 0.6		
	P051436104303	59984.25	2456	758.5 ± 0.6		
	P051436104304	59984.39	2557	745.1 ± 0.5		206.18 ± 0.44
	P051436104305	59984.52	2864	763.7 ± 0.5		
	P051436104307	59984.78	2609	725.3 ± 0.5		206.29 ± 0.52
	P051436104308	59984.91	415	637.2 ± 1.2		
	P051436104309	59985.05	734	730.9 ± 1.0		
	P051436104310	59985.18	2484	734.5 ± 0.5		206.21 ± 0.41
	P051436104311	59985.31	2484	771.7 ± 0.6		
	P051436104312	59985.44	2711	707.6 ± 0.5		
	P051436104313	59985.57	1497	776.1 ± 0.7		206.16 ± 0.67
	P051436104314	59985.71	1445	754.2 ± 0.7		
	P0514361044	P051436104401	59985.87	1481		766.9 ± 0.7
P051436104402		59986.00	193	728.0 ± 1.9		
P051436104403		59986.13	2895	812.9 ± 0.5		
P051436104404		59986.30	2479	747.6 ± 0.5	206.11 ± 0.48	
P051436104405		59986.43	2731	751.7 ± 0.5		
P051436104406		59986.56	1442	700.8 ± 0.7		
P051436104407		59986.70	1449	743.0 ± 0.7	206.11 ± 0.33	
P051436104408		59986.83	1124	760.1 ± 0.8		
P051436104410		59987.09	240	691.4 ± 1.7		
P051436104411		59987.22	1371	730.1 ± 0.7		
P0514361045	P051436104502	59988.05	2041	702.3 ± 0.6	206.10 ± 0.45	
	P051436104503	59988.21	1518	780.7 ± 0.7		
P0514361046	P051436104602	59989.04	1357	729.1 ± 0.7	205.84 ± 1.17	
P0514361047	P051436104702	59990.03	3149	692.7 ± 0.5	206.00 ± 1.01	
P0514361048	P051436104802	59990.99	1923	742.7 ± 0.6	205.88 ± 1.84	
	P051436104803	59991.12	2569	664.2 ± 0.5		
	P051436104804	59991.25	1555	660.4 ± 0.7		
P0514361049	P051436104902	59992.64	2913	633.8 ± 0.5	205.54 ± 0.92	
	P051436104903	59992.77	565	765.8 ± 1.2		
P0514361050	P051436105002	59993.96	2217	746.8 ± 0.6	205.65 ± 0.61	
	P051436105003	59994.09	2607	627.9 ± 0.5		
P0514361051	P051436105101	59994.86	1006	683.8 ± 0.8	205.77 ± 1.61	
P0514361052	P051436105201	59995.92	2775	607.4 ± 0.5	205.63 ± 0.54	
	P051436105202	59996.07	2661	645.2 ± 0.5		
P0514361053	P051436105302	59998.19	2225	652.6 ± 0.5	205.43 ± 0.26	
	P051436105305	59998.58	2640	659.9 ± 0.5		
	P051436105307	59998.85	2454	598.6 ± 0.5		205.45 ± 0.38
	P051436105308	59998.98	2948	658.8 ± 0.5		
	P051436105309	59999.11	2453	615.1 ± 0.5		
P0514361054	P051436105401	59999.49	2157	618.2 ± 0.5	205.48 ± 0.29	
	P051436105402	59999.64	927	586.3 ± 0.8		
	P051436105403	59999.78	965	577.5 ± 0.8		
	P051436105404	59999.91	3155	588.7 ± 0.4		
	P051436105405	60000.04	3074	675.2 ± 0.5		205.38 ± 0.21
	P051436105406	60000.17	2621	592.4 ± 0.5		
	P051436105408	60000.43	1512	592.8 ± 0.6		
P0514361055	P051436105502	60001.29	1293	575.9 ± 0.7	205.34 ± 0.25	
	P051436105504	60001.56	2170	538.8 ± 0.5		
	P051436105505	60001.69	17	482.2 ± 5.4		
	P051436105506	60001.82	2663	559.2 ± 0.5		205.20 ± 0.83

to be continued

ObsIDs	ExpIDs	Start time (MJD)	Exposure time (s)	Count Rate (cts s <sup>-1</sup> )	Period (s)
	P051436105507	60001.95	1454	522.6 ± 0.6	
	P051436105508	60002.09	2998	536.1 ± 0.4	
P0514361056	P051436105601	60003.99	3666	496.0 ± 0.4	205.26 ± 0.32
	P051436105602	60004.13	2817	491.3 ± 0.4	
	P051436105603	60004.27	1208	462.5 ± 0.6	
	P051436105604	60004.40	3100	486.0 ± 0.4	
	P051436105605	60004.53	1841	482.1 ± 0.5	205.18 ± 0.30
	P051436105606	60004.66	822	526.1 ± 0.8	
	P051436105607	60004.80	3422	458.7 ± 0.4	
	P051436105608	60004.93	4760	447.4 ± 0.3	
P0514361057	P051436105701	60005.77	4116	428.1 ± 0.3	205.14 ± 0.39
	P051436105702	60005.92	3540	435.9 ± 0.4	
	P051436105703	60006.05	2965	455.7 ± 0.4	
P0514361058	P051436105801	60006.69	2894	415.2 ± 0.4	205.14 ± 0.42
	P051436105802	60006.84	3362	393.6 ± 0.3	
	P051436105803	60006.98	2843	435.1 ± 0.4	
P0514361059	P051436105901	60007.69	3131	355.4 ± 0.3	205.09 ± 0.60
	P051436105902	60007.84	3374	406.6 ± 0.3	
	P051436105903	60007.97	2793	412.9 ± 0.4	
P0514361060	P051436106001	60008.61	1200	404.4 ± 0.6	205.07 ± 0.38
	P051436106002	60008.76	3203	364.2 ± 0.3	
	P051436106003	60008.89	4452	354.4 ± 0.3	
P0514361061	P051436106101	60009.87	4262	329.4 ± 0.3	205.04 ± 0.48
	P051436106102	60010.02	2695	344.8 ± 0.4	
	P051436106103	60010.14	1239	305.3 ± 0.5	
P0514361064	P051436106401	60016.81	2507	229.7 ± 0.3	204.90 ± 0.90
	P051436106402	60016.95	1684	197.1 ± 0.3	
P0514361065	P051436106501	60018.13	3364	195.0 ± 0.2	204.91 ± 0.26
	P051436106502	60018.28	3262	199.2 ± 0.2	
	P051436106503	60018.41	267	201.0 ± 0.9	
P0514361066	P051436106601	60019.99	716	198.5 ± 0.5	204.78 ± 0.64
	P051436106602	60020.12	4287	171.3 ± 0.2	
	P051436106603	60020.26	2276	167.3 ± 0.3	
P0514361067	P051436106701	60021.77	1592	152.8 ± 0.3	204.73 ± 1.05
	P051436106702	60021.90	978	161.3 ± 0.4	
	P051436106703	60022.04	1797	139.7 ± 0.3	
P0514361068	P051436106802	60023.10	6181	136.6 ± 0.1	204.85 ± 0.48
P0514361071	P051436107101	60024.55	2266	136.8 ± 0.2	204.72 ± 1.24
	P051436107102	60024.69	1723	131.9 ± 0.3	
	P051436107103	60024.82	947	137.0 ± 0.4	
P0514361072	P051436107201	60026.01	2848	118.4 ± 0.2	204.74 ± 0.78
	P051436107202	60026.15	2242	117.9 ± 0.2	
	P051436107203	60026.28	1206	104.6 ± 0.3	
P0514361073	P051436107301	60027.79	775	108.2 ± 0.4	204.73 ± 1.27
	P051436107302	60027.93	1114	102.7 ± 0.3	
	P051436107303	60028.06	3513	103.6 ± 0.2	
P0514361074	P051436107401	60029.25	1028	86.1 ± 0.3	204.75 ± 1.69
	P051436107402	60029.39	2028	97.7 ± 0.2	
	P051436107403	60029.52	2434	104.2 ± 0.2	

Table B2: *NICER* observations log used in this paper. The count rates in the 2–10 keV energy range and the periods are listed.

ObsIDs	Start time (MJD)	Exposure time (s)	Count Rate (cts s <sup>-1</sup> )	Period (s)
5203610101	59942.79	3786	173.8 ± 0.2	208.03 ± 0.97
5203610102	59942.99	8256	201.4 ± 0.2	208.02 ± 0.18
5203610103	59944.15	6535	214.9 ± 0.2	207.99 ± 0.39
5203610104	59945.44	1985	242.2 ± 0.3	208.02 ± 0.36
5203610105	59946.03	5339	255.5 ± 0.2	207.96 ± 0.17
5203610106	59947.65	2697	258.4 ± 0.3	207.90 ± 1.73
5203610107	59948.04	2380	188.7 ± 0.3	207.91 ± 0.19
5203610108	59949.65	5525	226.0 ± 0.2	207.86 ± 0.47
5203610109	59950.02	15481	213.4 ± 0.1	207.87 ± 0.18
5203610110	59950.99	15256	198.5 ± 0.1	207.86 ± 0.23
5203610111	59952.02	7770	161.5 ± 0.1	207.84 ± 0.20
5203610112	59953.11	4771	160.0 ± 0.2	207.84 ± 0.22
5203610113	59954.16	3685	146.5 ± 0.2	207.81 ± 0.19
5203610114	59955.05	3745	125.2 ± 0.2	207.81 ± 0.41
5203610115	59956.02	2762	105.7 ± 0.2	207.85 ± 0.25
5203610116	59957.11	3601	97.2 ± 0.2	207.78 ± 0.39
5203610117	59958.08	2590	102.9 ± 0.2	...
5203610118	59959.18	1746	157.5 ± 0.3	...
5203610119	59960.34	1511	184.3 ± 0.3	...
5203610120	59961.44	1914	236.3 ± 0.4	...
5203610121	59962.21	1773	274.6 ± 0.4	...
5203610122	59963.37	1429	324.4 ± 0.5	...
5203610123	59964.02	1323	345.0 ± 0.5	...
5203610124	59965.25	3548	385.8 ± 0.3	207.60 ± 0.22
5203610125	59966.02	3455	408.6 ± 0.3	207.58 ± 0.16
5203610126	59967.05	1766	413.7 ± 0.5	207.53 ± 4.21
5203610127	59968.15	5312	449.4 ± 0.3	207.52 ± 0.22
5203610128	59969.11	4677	439.7 ± 0.3	207.46 ± 0.27
5203610129	59970.08	4556	495.7 ± 0.3	207.40 ± 0.15
5203610130	59971.18	5417	535.5 ± 0.3	207.35 ± 0.21
5203610131	59972.01	4454	650.2 ± 0.4	207.29 ± 0.15
5203610132	59973.05	4060	721.7 ± 0.4	207.21 ± 0.17
5203610133	59974.14	5354	757.2 ± 0.4	207.09 ± 0.19
5203610134	59975.11	3507	763.1 ± 0.5	206.93 ± 0.20
5203610135	59976.01	6989	805.9 ± 0.3	206.90 ± 0.15
5203610136	59977.05	5099	854.8 ± 0.4	206.79 ± 0.15
5203610137	59978.01	11959	799.3 ± 0.3	206.73 ± 0.26
5203610138	59979.17	5629	822.6 ± 0.4	206.62 ± 0.24
5203610139	59980.01	6194	749.7 ± 0.3	206.51 ± 0.20
5203610140	59981.11	7441	736.9 ± 0.3	206.44 ± 0.26
5203610141	59982.01	11313	715.4 ± 0.3	206.37 ± 0.16
5203610142	59983.05	7778	685.5 ± 0.3	206.30 ± 0.19
5203610143	59984.08	11269	660.9 ± 0.2	206.24 ± 0.23
5203610144	59985.50	4309	636.8 ± 0.4	206.14 ± 0.29
5203610145	59986.02	11726	638.9 ± 0.2	206.11 ± 0.17
5203610146	59987.24	2758	611.8 ± 0.5	206.05 ± 0.29
5203610147	59988.02	3868	631.0 ± 0.4	206.00 ± 0.15
5203610148	59989.00	6620	611.5 ± 0.3	205.95 ± 0.20
5203610149	59990.02	15075	594.5 ± 0.2	205.89 ± 0.16
5203610150	59991.11	9389	562.5 ± 0.2	205.84 ± 0.22
5203610151	59992.22	2463	569.0 ± 0.5	205.77 ± 0.25
5203610152	59993.19	4163	572.2 ± 0.4	205.73 ± 0.23
5203610153	59994.01	6335	553.5 ± 0.3	205.69 ± 0.17
5203610154	59995.04	9434	546.1 ± 0.2	205.64 ± 0.23
5203610158	60001.29	2181	559.5 ± 0.5	205.31 ± 0.51
6203610101	60005.66	1605	407.8 ± 0.5	205.22 ± 1.15

to be continued

ObsIDs	Start time (MJD)	Exposure time (s)	Count Rate (cts s <sup>-1</sup> )	Period (s)
6203610102	60006.44	1088	450.9 ± 0.6	...
6203610103	60007.03	5405	411.2 ± 0.3	205.11 ± 0.16
6203610104	60008.37	3789	405.3 ± 0.3	205.07 ± 0.35
6203610105	60009.21	6983	390.5 ± 0.2	205.06 ± 0.33
6203610106	60010.31	2590	369.2 ± 0.4	205.03 ± 0.32
6203610107	60011.21	6722	346.0 ± 0.2	204.99 ± 0.20
6203610108	60012.24	5292	334.4 ± 0.3	205.01 ± 0.47
6203610109	60013.03	3094	324.2 ± 0.3	204.96 ± 0.24
6203610110	60014.06	4442	314.6 ± 0.3	204.93 ± 0.25
6203610111	60015.02	3190	309.1 ± 0.3	204.91 ± 0.26
6203610112	60016.12	3013	284.8 ± 0.3	204.89 ± 0.22
6203610113	60017.21	2999	266.6 ± 0.3	204.90 ± 0.28
6203610114	60018.18	3628	274.3 ± 0.3	204.87 ± 0.26
6203610115	60019.20	7252	237.3 ± 0.2	204.87 ± 0.63
6203610116	60020.04	13922	234.0 ± 0.1	204.84 ± 0.16
6203610117	60021.08	8270	224.0 ± 0.2	204.83 ± 0.17
6203610118	60021.98	7739	202.4 ± 0.2	204.82 ± 0.16
6203610119	60023.15	8534	199.0 ± 0.2	204.81 ± 0.15
6203610120	60023.98	7635	204.8 ± 0.2	204.81 ± 0.11
6203610121	60025.10	10040	192.3 ± 0.1	204.79 ± 0.25
6203610122	60025.99	6237	203.7 ± 0.2	204.79 ± 0.14
6203610123	60027.01	7786	147.6 ± 0.1	204.78 ± 0.11
6203610124	60028.00	7271	167.4 ± 0.2	204.78 ± 0.18
6203610125	60029.02	7916	162.9 ± 0.1	204.78 ± 0.15
6203610126	60030.05	3230	155.0 ± 0.2	204.80 ± 0.23
6203610127	60031.08	4044	123.1 ± 0.2	204.78 ± 0.20

This paper has been typeset from a  $\text{\TeX}/\text{\LaTeX}$  file prepared by the author.